ORIGINAL PAPERS

Improved carrier dynamics in nickel/urea-functionalized carbon nitride for ethanol photoreforming

Denny Gunawan[1] · Cui Ying Toe[1,2] · Kaiwen Sun[3] · Jason Scott[1] · Rose Amal[1]

Abstract

Photoreforming has been shown to accelerate the H_2 evolution rate compared to water splitting due to thermodynamically favorable organic oxidation. In addition, the potential to simultaneously produce solar fuel and value-added chemicals is a significant benefit of photoreforming. To achieve an efficient and economically viable photoreforming process, the selection and design of an appropriate photocatalyst is essential. Carbon nitride is promising as a metal-free photocatalyst with visible light activity, high stability, and low fabrication cost. However, it typically exhibits poor photogenerated charge carrier dynamics, thereby resulting in low photocatalytic performance. Herein, we demonstrate improved carrier dynamics in urea-functionalized carbon nitride with in situ photodeposited Ni cocatalyst (Ni/Urea-CN) for ethanol photoreforming. In the presence of 1 mM Ni^{2+} precursor, an H_2 evolution rate of 760.5 μmol h^{-1} g^{-1} and an acetaldehyde production rate of 888.2 μmol h^{-1} g^{-1} were obtained for Ni/Urea-CN. The enhanced activity is ascribed to the significantly improved carrier dynamics in Urea-CN. The ability of oxygen moieties in the urea group to attract electrons and to increase the hole mobility via a positive shift in the valence band promotes an improvement in the overall carrier dynamics. In addition, high crystallinity and specific surface area of the Urea-CN contributed to accelerating charge separation and transfer. As a result, the electrons were efficiently transferred from Urea-CN to the Ni cocatalyst for H_2 evolution while the holes were consumed during ethanol oxidation. The work demonstrates a means by which carrier dynamics can be tuned by engineering carbon nitride via edge functionalization.

Graphical abstract
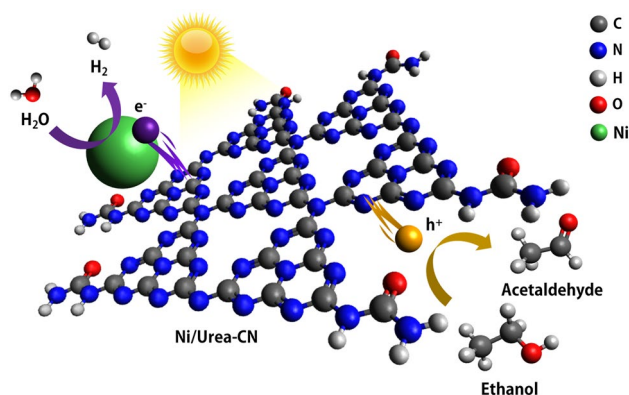
✉ Cui Ying Toe
cuiying.toe@newcastle.edu.au

✉ Rose Amal
r.amal@unsw.edu.au

Extended author information available on the last page of the article

1 Introduction

Photocatalysis offers a direct route to harness solar energy for green H_2 production. Water splitting over a semiconductor photocatalyst, for instance, has been extensively demonstrated to cogenerate H_2 and O_2 [1]. Compared to photovoltaic-powered electrolysis, this process is expected to offer lower capital and operating expenditure as solar panels and expensive electrolyzers are not needed [2–4]. In addition, this technology can be employed remotely and for onsite use, reducing the reliance on long distance H_2 transport [5]. However, the application of photocatalytic water splitting is hindered by the challenging O_2 evolution reaction that ultimately leads to poor solar-to-H_2 conversion efficiency [6].

Photoreforming is a promising alternative to photocatalytic water splitting in which the O_2 evolution reaction is replaced with a thermodynamically favorable organic oxidation reaction. This process has been shown to significantly accelerate the H_2 evolution reaction [7]. Nevertheless, typical photoreforming may generate CO_2 waste from over-oxidation of the organic substrate. For example, a Pt/TiO_2 photocatalyst has been shown to achieve an H_2 evolution rate of 10.5 mmol h^{-1} g^{-1} during the photoreforming of methanol with 45% selectivity toward CO_2 [8]. Consequently, controlling the extent to which organic oxidation occurs is crucial to achieving selective photoreforming. Delivering a selective system would enable the simultaneous production of solar H_2 fuel and value-added chemicals [9].

Ethanol, obtained from waste biomass such as brewery and food industry wastewater, is an appealing organic substrate for photoreforming, particularly due to difficult separation of the ethanol–water azeotropic mixture. In addition to its proven role in accelerating the H_2 evolution rate, utilizing waste-derived ethanol can significantly contribute to lowering the H_2 production cost while alleviating the waste issue at the same time. However, due to its simple chemical structure, ethanol is relatively easy to be over-oxidized into CO_2 and/or undergo side reactions into undesirable CO, CH_4, and C_2H_4 products. Consequently, controlling the selectivity of ethanol oxidation to a high value intermediary product, such as acetaldehyde, is crucial. Acetaldehyde is widely used as an industrially important feedstock to manufacture a multitude of end products including food and beverages, paints and coatings, adhesives, resins, and pharmaceuticals [10]. In 2020, the acetaldehyde market was valued at US\$1,567.84 million and is projected to reach US\$2,422.75 million by 2030 [11], thus highlighting a significant economic benefit of selective ethanol photoreforming.

Generally, most visible-light-responsive semiconductors are compelling photocatalyst candidates for selective photoreforming by virtue of their suitable band edges to drive H_2 evolution and to prevent the formation of non-selective hydroxyl radicals. Graphitic carbon nitride (g-C_3N_4) is one in a suite of visible-light-active semiconductor materials that has gained substantial attention for selective photoreforming due to its high stability and low fabrication cost [12]. More importantly, the unique characteristics of polymeric carbon nitride allow for a facile surface engineering at a molecular level [13]. However, the photocatalytic performance of carbon nitride is restricted by its poor charge carrier separation and utilization. In general, pristine carbon nitride has several shortcomings, such as large particle size, high recombination rate of charge carriers, and low electrical conductivity [14].

To date, the photocatalytic efficiency of carbon nitride, indicated by apparent quantum yield (AQY) and solar-to-H_2 conversion efficiency (STH), does not meet practical needs. The AQY of carbon nitride photocatalysts, which reflects the quality of the light-harvesting materials, remains low especially when compared to inorganic semiconductors. In terms of STH, the highest reported STH efficiency for carbon nitride-based photocatalysts is around 2% [15], which is lower than the 10% STH practical feasibility threshold defined by the U.S. Department of Energy. Enhancing carrier dynamics in carbon nitride is key to improving both the AQY and STH which is essential to increase the viability. A range of photocatalyst design strategies, such as nanostructuring, doping, copolymerization, functionalization, defect engineering, and heterojunction formation have been developed to improve the activity of carbon nitride [16–20]. Among them, surface functionalization has been demonstrated as a promising technique to suppress electron–hole recombination in carbon nitride by inducing an uneven charge distribution. Cyanamide-functionalized carbon nitride, for example, was reported to be more effective in transferring the holes for organic oxidation, thus leading to an enhanced electron uptake for H_2 production [21, 22]. More recently, urea-functionalized carbon nitride derived from cyanamide-terminated carbon nitride has been found to further improve photocatalytic H_2 evolution performance although it is less studied compared to other functionalized carbon nitrides [23].

In addition to a functionalization strategy, cocatalysts can play a crucial role in accelerating charge carrier dissociation and providing catalytically active sites for the H_2 evolution reaction. Platinum, for instance, is a prominent metal cocatalyst that has been demonstrated to significantly boost the H_2 evolution rate. However, using expensive Pt metal can increase process costs and promote C–C cleavage of organics that leads to undesirable over-oxidation into CO_2 [24]. Alternatively, Ni has been shown as a promising and comparatively inexpensive metal cocatalyst for both H_2 production and selective alcohol oxidation. On

a cyanamide-functionalized carbon nitride, in situ photodeposited Ni cocatalyst in the presence of excess Ni^{2+} ions was previously reported to give an H_2 production rate of 2.32 mmol h^{-1} g^{-1} and an acetaldehyde production rate of 2.54 mmol h^{-1} g^{-1} with negligible CO_2 production [21]. However, slow Ni photodeposition was observed as indicated by a 4 h lag time at the start of the reaction due to the strong electron-storing property of cyanamide-functionalized carbon nitride and the energetically challenging Ni^{2+} reduction process [21].

Here, we report the use of urea-functionalized carbon nitride with in situ photodeposited Ni for ethanol photoreforming. The presence of urea groups is expected to siginificantly shorten the lag time for Ni^{2+} reduction as well as increase the H_2 evolution and acetaldehyde production rates due to the improved photogenerated charge carrier dynamics. The promotional effects of the urea functional groups and Ni cocatalyst during ethanol photoreforming are investigated using extensive photocatalytic studies and in-depth photoelectrochemical characterization. The findings offer new insights into how carbon nitride functionality influences its charge carrier dynamics as well as electron transfer to the metal cocatalyst, thus collectively enhancing the photocatalytic activity.

2 Experimental

2.1 Chemicals

Melamine (99%), potassium thiocyanate (KSCN, 99%), and nickel nitrate hexahydrate $(Ni(NO_3)_2 \cdot 6H_2O$, 99.999%) were obtained from Sigma-Aldrich. Ethanol (100%) was purchased from ChemSupply. Prior to use, KSCN was dried at 140 °C under vacuum. All other chemicals were used as received without further purification.

2.2 Photocatalyst synthesis

Pristine carbon nitride (p-CN) was synthesized via polymerization of the melamine precursor at 550 °C for 4 h under air in a muffle furnace. Cyanamide-functionalized carbon nitride (NCN-CN) was fabricated by grinding p-CN and KSCN (weight ratio 1:2) and heating the solid mixture at 400 °C for 1 h followed by 500 °C for 30 min under Ar in a horizontal tube furnace [25]. After being naturally cooled to ambient temperature, the obtained product was washed with water multiple times and dried at 60 °C under vacuum.

Urea-functionalized carbon nitride (Urea-CN) was prepared by adding 500 mg of NCN-CN to 50 mL of 1 M HCl aqueous solution. After 2 h of stirring, the resulting off-white mixture was centrifuged, washed repeatedly with water, and dried at 60 °C in a vacuum oven.

2.3 Photocatalyst characterization

Attenuated total reflectance infrared (ATR-IR) spectra were acquired on a PerkinElmer UATR Spectrum Two Fourier transform infrared (FTIR) spectrometer with a diamond crystal. X-ray photoelectron spectroscopy (XPS) was undertaken on a Thermo ESCALAB250Xi instrument with Al Kα radiation source. X-ray diffraction (XRD) patterns were obtained on a PANalytical X'Pert multipurpose diffractometer, using Cu Kα radiation at 45 kV and 40 mA. Brunauer–Emmett–Teller (BET) surface areas were measured on a Micromeritics TriStar 3030 instrument using the N_2 physisorption method at − 195.8 °C. The samples were degassed under vacuum at 150 °C for 3 h prior to analysis. UV–Vis diffuse reflectance spectra (DRS) were recorded on a Shimadzu UV-3600 spectrophotometer with $BaSO_4$ as the reference and analyzed using the Kubelka–Munk model. Photoluminescence (PL) spectra of the sample dispersed in water (250 mg L^{-1}) were collected on a HORIBA Fluoromax-4 spectrofluorometer at an excitation wavelength of 318 nm. Time-resolved photoluminescence (TRPL) characterization was carried out on the p-CN, NCN-CN, and Urea-CN thin films using time-correlated single photon counting (TCSPC) (Microtime200, Picoquant) with excitation wavelength of 405 nm at a repetition rate of 10 MHz. To exclude the signals from excitation laser, a 430–490 nm band pass filter was applied before the detector. The metal loading on the powder samples was measured using a PerkinElmer OPTIMA 7300 inductively coupled plasma-atomic emission spectrometer (ICP-AES) after microwave-assisted aqua regia digestion.

Photoelectrochemical (PEC) characterization was carried out in a cell equipped with a quartz window for illumination using an Autolab potentiostat (PGSTAT204). The electrolyte was a mixture of 10% ethanol and 90% 0.5 M Na_2SO_4 aqueous solution. Ag/AgCl and Pt foil were utilized as the reference and counter electrodes, respectively. The working electrode was prepared by drop casting the sample suspension in ethanol (2 mg cm^{-2}) on a fluorine-doped tin oxide (FTO) slide (2×1 cm^2). Chronoamperometry was undertaken under chopped illumination by a solar simulator (Newport, 100 mW cm^{-2}) at a potential of 1.2 V *vs* RHE. Electrochemical Mott–Schottky plots were obtained under dark condition with the potential ranging from − 0.2 to 1.0 V vs RHE and a frequency of 1000 Hz. Electrochemical impedance spectra (EIS) were acquired in the dark under a potential of 0 V vs RHE and a frequency from 0.1 Hz to 100 kHz. Linear sweep voltammetry (LSV) was carried out under dark conditions with an applied voltage from − 0.8 to 0.0 V vs RHE.

Scheme 1 Schematic illustration of Urea-CN synthesis, showing p-CN and its conversion to NCN–CN by an ionothermal treatment using KSCN melt, and its acid-catalyzed hydrolysis to Urea-CN. Edge functional groups in p-CN, NCN-CN, and Urea-CN are highlighted in yellow
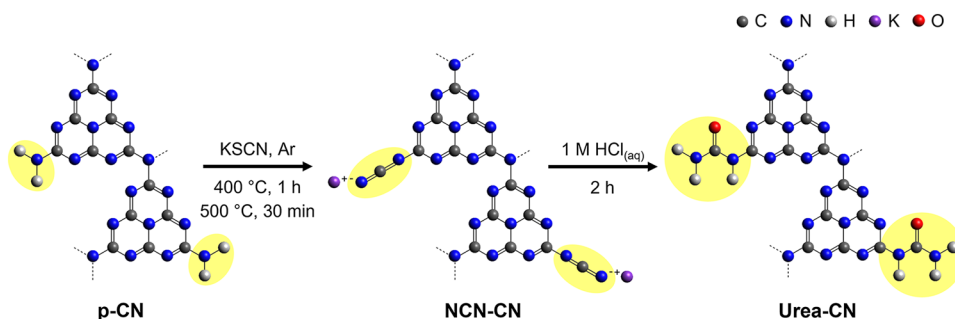
2.4 Evaluation of photoreforming performance

Photoreforming tests were conducted in a spiral photoreactor as illustrated in Fig. S1 [21, 26] (illumination area ~ 218.4 cm^2). A 100 mg load of photocatalyst was dispersed in 100 mL of 10 vol % ethanol and 1 mM $Ni(NO_3)_2 \cdot 6H_2O$ aqueous solution under ultrasonication. The mixture was added to the photoreactor and purged with N_2 prior to light irradiation. All tests were performed under illumination using a 20 W NEC fluorescent lamp FL20SBL (light intensity ~ 5 mW cm^{-2}) as the light source. Figure S2 shows the emission spectrum of the lamp.

Gaseous products including H_2, CH_4, CO, CO_2, and C_2H_4 were analyzed using an online Shimadzu GC-2014 gas chromatograph equipped with a thermal conductivity detector (TCD) and flame ionization detector (FID). After a defined reaction time, liquid samples were withdrawn from the photoreactor, filtered through a 0.22 µm nylon syringe filter, mixed with D_2O (volume ratio of liquid sample to D_2O was 9:1), and analyzed by ^1H nuclear magnetic resonance (NMR) spectroscopy on a Bruker Avance III 600 MHz NMR using a presaturation method for water suppression. The external standard was sodium acetate in H_2O/D_2O (volume ratio of 9:1).

2.5 Ferrioxalate actinometry

Ferrioxalate actinometry was performed on the spiral photoreactor. The actinometry was conducted using the protocol descsribed by Hatchard and Parker [27]. The reactor was filled with 100 mL of 6.1 mM potassium ferrioxalate and 0.05 M sulfuric acid solution. The kinetics of Fe^{2+} formation under light irradiation were followed by periodically withdrawing a 20 µL aliquot from the reactor and mixing it with 5.75 mL of 1 M sodium acetate, 3.75 mL of 0.5 M sulfuric acid, and 125 µL of ligand solution (0.05 M 1,10-phenanthroline and 0.05 M sulfuric acid). The concentration of Fe^{2+} was determined from the absorbance at 510 nm (Shimadzu UV-3600 spectrophotometer). The calibration curve was obtained using Mohr's salt as the Fe^{2+} standard.

3 Results and discussion

Urea-functionalized carbon nitride (Urea-CN) was prepared via a two-step treatment procedure as shown in Scheme 1. In the first step, the pristine carbon nitride (p-CN) prepared via thermal polymerization of melamine was further treated with KSCN at 400 °C for 1 h and 500 °C for 30 min under an Ar atmosphere to form cyanamide-functionalized carbon nitride (NCN-CN). Subsequently, the cyanamide groups in NCN-CN undergo an acid hydrolysis reaction upon the addition of HCl aqueous solution to form Urea-CN.

The synthesized p-CN is a typical heptazine-based carbon nitride as indicated by the presence of heptazine rings and bridging secondary amines (-C-N) observed from its ATR-IR spectrum in Fig. 1a. The IR vibration at 803 cm^{-1} corresponds to the heptazine core, while the IR bands at 1307 and 1211 cm^{-1} confirm the existence of –C–N [25, 28]. Upon ionothermal and acid-catalyzed hydrolysis, both NCN–CN and Urea-CN maintain their natures as heptazine-based carbon nitride materials, evidenced by the IR bands for heptazine rings and –C–N. In terms of edge functionality, amino groups are present on the surface of p-CN as revealed by the N–H stretching IR vibration at 3000 cm^{-1}. On NCN–CN, the amino functional groups were substituted by the cyanamide groups as shown by the C≡N stretching IR vibration band at 2181 cm^{-1} [25]. After the acid hydrolysis treatment, the cyanamide groups were hydrolyzed into urea functional groups as indicated by suppression of the C≡N band as well as the appearance of characteristic IR bands for urea at 1653, 1579, and 1549 cm^{-1} [23]. In addition, the presence of urea groups in Urea-CN is confirmed by the appearance of a C=O peak (533.4 eV) in its O 1 s XPS spectrum which does not exist at the O 1 s edge of p-CN and NCN–CN (Fig. S3).

Figure 1b shows that p-CN has the most prominent diffraction peak at 27.6° which is denoted as the (002) plane with a *d*-spacing of 3.23 Å. This peak is ascribed to the interlayer distance of the graphitic material. p-CN also exhibits a low-angle reflection peak at 12.8°, indexed as the (100) plane with an in-plane periodicity of 6.90 Å. The peak corresponds to the distance of the nitride pores [25]. The XRD pattern of NCN–CN suggests a denser plane stacking for

Fig. 1 Physicochemical characterization of p-CN, NCN-CN, and Urea-CN. **a** ATR-IR spectra and **b** XRD patterns of p-CN, NCN–CN, and Urea-CN
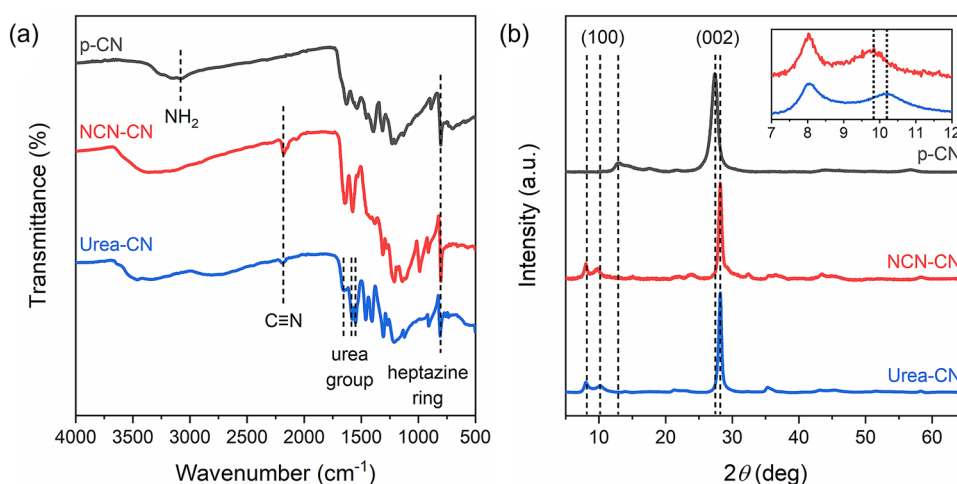
NCN–CN with an interlayer distance of 3.16 Å as indicated by the (002) peak shift to a higher angle of 28.3°. In addition, the (100) peak of NCN–CN is split and shifted to 8.0 and 9.8°, revealing extended in-plane distances of 11.0 and 9.02 Å, respectively. Urea-CN, which is derived from NCN-CN, exhibits similar XRD features to NCN–CN, suggesting that the acid hydrolysis did not alter the bulk crystal structure. However, one notable difference is a slight shift of the (100) peak from 9.8° to 10.2°, implying a smaller d-spacing for Urea-CN (8.67 Å). This could be attributed to the ability of urea functional groups to form hydrogen bonds with the surrounding heptazine rings, leading to tighter packing [23].

The influences of edge functional group in carbon nitride on the electronic band structure were investigated using a suite of characterization techniques including UV–Vis DRS, Mott–Schottky measurements, and valence band XPS.

Figure 2a illustrates that p-CN and NCN-CN have similar band gap energies of 2.67 and 2.69 eV, respectively. However, the conversion of cyanamide groups to urea groups was observed to significantly widen the band gap energy to 2.83 eV. Valence band XPS was undertaken to determine the energy difference between the Fermi level and valence band [29]. Values of 2.36, 2.15, and 2.75 eV were obtained for p-CN, NCN–CN, and Urea-CN, respectively (Fig. S4). Mott–Schottky measurements were also conducted to estimate the flat band potentials of the samples. The positive slopes of the Mott–Schottky plots (Fig. S5) for all samples indicates that they are n-type semiconductors and the flat band potentials can be assumed to be the same as the Fermi levels [30]. As shown in Fig. S5, Fermi levels of -0.38, -0.36, and -0.44 V vs RHE were observed for p-CN, NCN–CN and Urea-CN, respectively. Combining all the
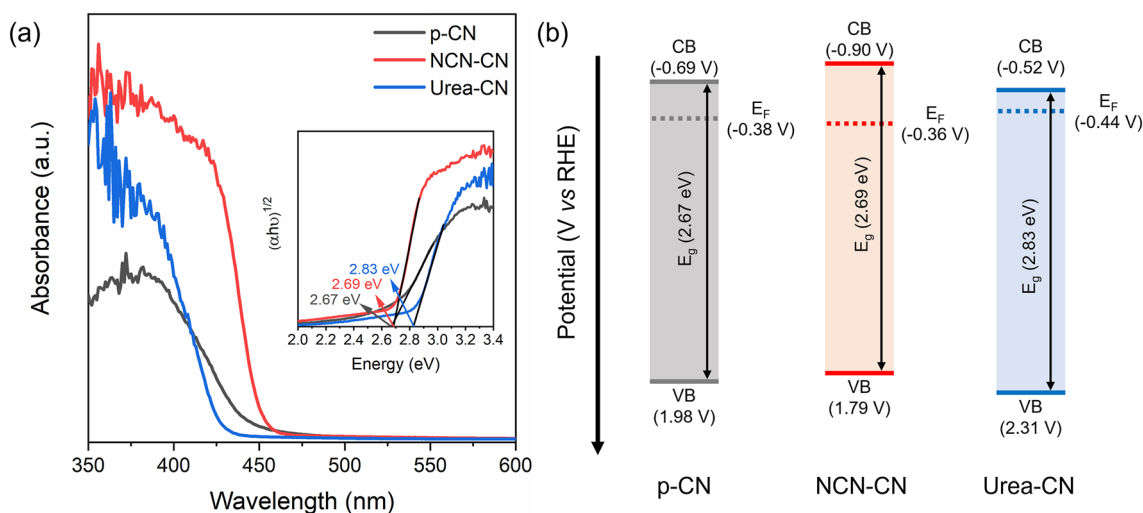

Fig. 2 Electronic band structure arrangements for p-CN, NCN–CN, and Urea-CN. **a** UV–Vis DRS spectra of p-CN, NCN–CN, and Urea-CN with the corresponding Tauc plots in the inset. **b** Schematic illustration of the postulated electronic band structures of p-CN, NCN–CN, and Urea-CN

above information, the band structures of p-CN, NCN–CN, and Urea-CN are postulated as illustrated in Fig. 2b. It is apparent that Urea-CN possesses a more energetic valence band than p-CN and NCN–CN. This is due to the contribution of the O 2p orbital from the urea functionality that leads to the shift in the valence band toward a more positive value [31].

The role of edge functionality in determining the photocatalytic activity and selectivity of the samples for ethanol photoreforming was evaluated. Urea-CN exhibits improved H_2 production compared to p-CN and NCN–CN as illustrated in the time-dependent H_2 evolution profiles (Fig. 3a). Figure 3b shows that p-CN generated 24.3 µmol h^{-1} g^{-1} of H_2 and 36.0 µmol h^{-1} g^{-1} of acetaldehyde with an acetaldehyde selectivity of 96.6%. Upon cyanamide functionalization, NCN–CN exhibited an enhanced acetaldehyde production of 155.1 µmol h^{-1} g^{-1} with close to 100% selectivity toward acetaldehyde. The negligible H_2 production from NCN-CN is attributed to its electron-storing capability [32, 33]. In contrast, the introduction of urea groups on Urea-CN was found to improve the H_2 evolution rate to 44.7 µmol h^{-1} g^{-1} and increase the acetaldehyde production rate to 175.6 µmol h^{-1} g^{-1} with an acetaldehyde selectivity of 97.6%. The lower H_2 yield compared to the acetaldehyde yield for the Urea-CN photocatalyst is likely ascribed to the remaining cyanamide groups that are not hydrolyzed as shown by the residual C≡N stretching IR vibration band in Fig. 1a. This indicates that a portion of the electrons generated by Urea-CN is stored within the remaining cyanamide moieties, lowering the overall electron uptake for the surface reduction reaction.

To improve the electron uptake and enhance the overall performance, Ni was in situ photodeposited on p-CN, NCN–CN, and Urea-CN. The initial concentration of Ni^{2+} was maintained at 1 mM and the samples are denoted as Ni/p-CN, Ni/NCN-CN, and Ni/Urea-CN, respectively. The time-dependent H_2 evolution profiles in Fig. 4a show that, upon the introduction of Ni^{2+}, lag periods at the beginning of the reaction due to the Ni photodeposition process are present for all three samples. For Ni/p-CN, a lag period of 1 h is observed followed by poor H_2 evolution and acetaldehyde production rates of 102.6 and 282.0 µmol h^{-1} g^{-1}, respectively (Fig. 4b). The short lag time for p-CN accompanied by poor performance indicates a weak interaction between the Ni cocatalyst and amino groups present on p-CN. In contrast, Ni/NCN–CN exhibits the longest induction time of 4 h, which may be attributed to the strong electron-storing property of NCN–CN. The ensuing performance of Ni/NCN-CN (201.6 µmol H_2 h^{-1} g^{-1} and 352.5 µmol acetaldehyde h^{-1} g^{-1}) is higher than for Ni/p-CN. The improved photocatalytic activity of Ni/NCN–CN compared to Ni/p-CN is driven by the role of cyanamide groups in invoking effective photogenerated hole transfer to the ethanol, as discussed in our previous study [21]. This leads to a higher electron uptake by the Ni species for self-reduction into Ni deposits and subsequently, for H_2 generation. Moreover, cyanamide groups in NCN–CN were found to be a better ligand for Ni attachment on the surface compared to amino groups in p-CN, providing a stronger metal–support interaction. This is evidenced by the higher Ni loading of Ni/NCN–CN (5.87 wt %) compared to Ni/p-CN (0.97 wt %) [21, 25].

Unlike Ni/NCN–CN, Ni/Urea-CN offers a shorter lag period of 1 h. Interestingly, the photocatalytic performance was significantly enhanced with H_2 and acetaldehyde production rates of 760.5 and 888.2 µmol h^{-1} g^{-1}, respectively. Despite the lower actual Ni loading on the Ni/Urea-CN
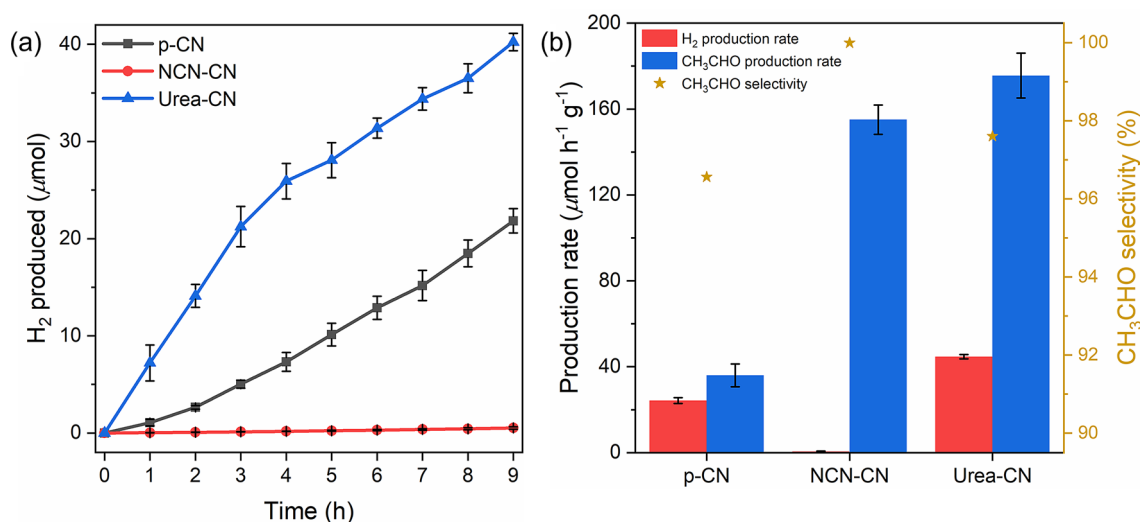

Fig. 3 Ethanol photoreforming performance by p-CN, NCN–CN, and Urea-CN. **a** Time-dependent H_2 evolution profiles and **b** calculated H_2 and acetaldehyde production rates for p-CN, NCN–CN, and Urea-CN
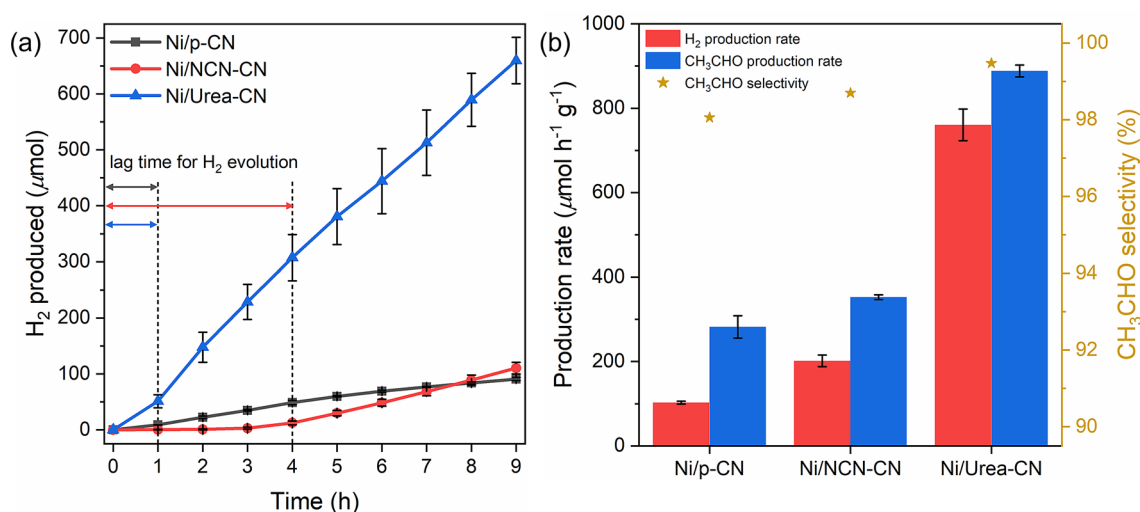
Fig. 4 Ethanol photoreforming performance by Ni/p-CN, Ni/NCN-CN, and Ni/Urea-CN. **a** Time-dependent H_2 evolution profiles and **b** calculated H_2 and acetaldehyde production rates for Ni/p-CN, Ni/NCN–CN, and Ni/Urea-CN

photocatalyst (0.97 wt %), its performance exceeds the activity for Ni/NCN–CN. The presence of Ni cocatalyst on Urea-CN is further confirmed by the Ni 2p XPS spectra as shown in Fig. S6, which indicates Ni^0 (853.6 eV) and Ni^{2+} (856.3 and 858.4 eV) species are present [34, 35]. The higher acetaldehyde yield for Ni/Urea-CN than that obtained for Ni/p-CN and Ni/NCN–CN is attributed to its more energetic valence band (although it is still insufficient for nonselective hydroxyl radical formation) that leads to a higher hole mobility. In terms of H_2 production, the enhancement shown by Ni/Urea-CN is also significantly higher than for Ni/p-CN and Ni/NCN–CN. This is ascribed to the presence of the O atom in the urea groups which may improve charge carrier dynamics in Urea-CN, thus accelerating electron transfer from Urea-CN to the Ni cocatalyst. In this instance, Ni holds a crucial role in delivering higher activity due to several factors. When Ni is anchored on Urea-CN, a junction will form due to the higher work function of Ni than carbon nitride [36]. The junction leads to the effective transfer of photoexcited electrons from Urea-CN to Ni. Moreover, Ni acts as the active site for proton reduction into H_2, thus lowering the reaction energy barrier, which in turn improves H_2 production [36].

In addition to the H_2 evolution rate, the AQY, which is widely approved as a benchmark parameter in the photocatalysis field [37–39], was calculated. It should be pointed out that the AQY in this work was obtained only for one photocatalyst loading (1 mg mL^{-1}) that has not been optimized yet. In photocatalytic H_2 generation, AQY is defined as the ratio of the number of photogenerated electrons applied for H_2 evolution relative to the number of incident photons on the photocatalyst from outside [39]. As a polychromatic light source was used in this work, ferrioxalate actinometry

was employed to estimate the number of incident photons ($\lambda = 250$–500 nm) on the spiral photoreactor (Supplementary Methods). Figure S7 shows that the spiral photoreactor used in this work exhibits a high photon flux of 2.860×10^{18} photons s^{-1} despite the low intensity of the light source. This highlights the benefit of a spiral photoreactor in that it provides a high exposed light illumination area (~ 218.4 cm^2), thus allowing for a high number of incident photons at low light intensity. Based on the obtained photon flux and H_2 evolution rate, the AQY was calculated using Eq. 1 [39].

$$AQY = \frac{2 \times r_{H_2}}{n}, \qquad (1)$$

where r_{H_2} is the H_2 evolution rate (mol s^{-1}) and n is incident photon flux. The unoptimized AQY for Ni/Urea-CN (0.89%) is higher than for Ni/p-CN (0.12%) and Ni/NCN–CN (0.24%), thereby indicating more efficient light utilization for H_2 evolution by Ni/Urea-CN. When compared to the existing literature on Ni/g-C$_3$N$_4$-based photocatalysts (Table S3), the calculated AQY in this work is relatively low. This may be attributed to the unoptimized photocatalyst and cocatalyst loadings, which strongly influence the AQY value [39]. Nevertheless, the unoptimized AQYs for Ni/p-CN, Ni/NCN–CN, and Ni/Urea-CN in this work are sufficient to confirm the improved charge carrier dynamics in Ni/Urea-CN.

To provide insights into material stability, long-term ethanol photoreforming was performed for Ni/Urea-CN. The Ni^{2+} precursor was introduced only at the beginning of the first cycle and with no additional Ni^{2+} then added in the subsequent cycles. The long-term time-dependent H_2 evolution profile in Figure S8 shows a moderate stability

in terms of H$_2$ generation with a decrease in H$_2$ yield under a prolonged irradiation time. To investigate factors influencing the stability, Ni/Urea-CN was recovered after 9 h of reaction and characterized by ATR-IR spectroscopy. As seen in Figure S9, the ATR-IR spectrum of Ni/Urea-CN is nearly identical to that of fresh Urea-CN, indicating that urea groups remained. However, a new strong IR band at 1223 cm^{-1}, which is likely to be attributed to C–O stretching vibration, was observed after reaction. The appearance of C–O stretching IR vibration in Ni/Urea-CN suggests that a portion of urea functional groups was hydrolyzed during the longer reaction timeframe, leading to a decrease in the long-term photocatalytic performance.

As our previous findings suggest that excess Ni^{2+} in solution may also impart a significant effect on the performance of the carbon nitride photocatalyst, we performed a control experiment using a 1 wt % Ni^{2+} precursor on Urea-CN (close to the actual Ni loading on Ni/Urea-CN), which is denoted as Ni(1%)/Urea-CN. Figure S10 shows that Ni(1%)/Urea-CN exhibits a longer induction period and lower performance compared to Ni/Urea-CN, indicating there are charge-induced activation effects invoked by the excess Ni^{2+} in solution as was observed in our previous work. However, it is interesting to see that, even with a low Ni^{2+} input, the H$_2$ evolution rate for Ni(1%)/Urea-CN (390.9 µmol h^{-1} g^{-1}) is twofold higher than for Ni/NCN-CN (which has Ni cocatalyst loading of 5.87 wt %). Consequently, it is important to investigate the charge carrier dynamics of all samples to determine the factor(s) that improve ethanol photoreforming performance in the presence of the Ni cocatalyst.

In-depth photoelectrochemical characterization was conducted to confirm the accelerated carrier dynamics in the Urea-CN photocatalyst. Steady-state PL spectra, shown in Fig. 5a, illustrate a strong emission signal for p-CN which originates from the radiative decay of charge carriers in the heptazine matrix due to electron–hole recombination [40]. In contrast, both NCN–CN and Urea-CN exhibit a significant quenching of emission peaks in which the signal for Urea-CN is the lowest. The emission peak for Urea-CN is also shifted to a shorter wavelength (412 nm) compared to p-CN and NCN-CN (445 nm) due to the wider band gap of Urea-CN. In addition, upon grafting the urea groups, the chronoamperometric I–t plots with chopped illumination in Fig. 5b show that Urea-CN has the best photoresponse among the three samples with a photocurrent density of 47.5 µA cm^{-2} at an applied potential of 1.0 V vs RHE. Collectively, the reduced PL emission intensity and improved photocurrent density displayed by Urea-CN reveals better

Fig. 5 Charge carrier dynamics in p-CN, NCN-CN, Urea-CN and Ni/Urea-CN. **a** Steady-state PL spectra for p-CN, NCN–CN, and Urea-CN. **b** Chronoamperometry I–t curves for p-CN, NCN–CN, and Urea-CN under chopped illumination at 1.2 V vs RHE. **c** Electrochemical impedance spectra (EIS) for p-CN, NCN–CN, and Urea-CN under the dark condition at an applied potential of 0.0 V vs RHE. **d** Cathodic linear sweep voltammetry (LSV) curves for Urea-CN and Ni/Urea-CN under the dark condition
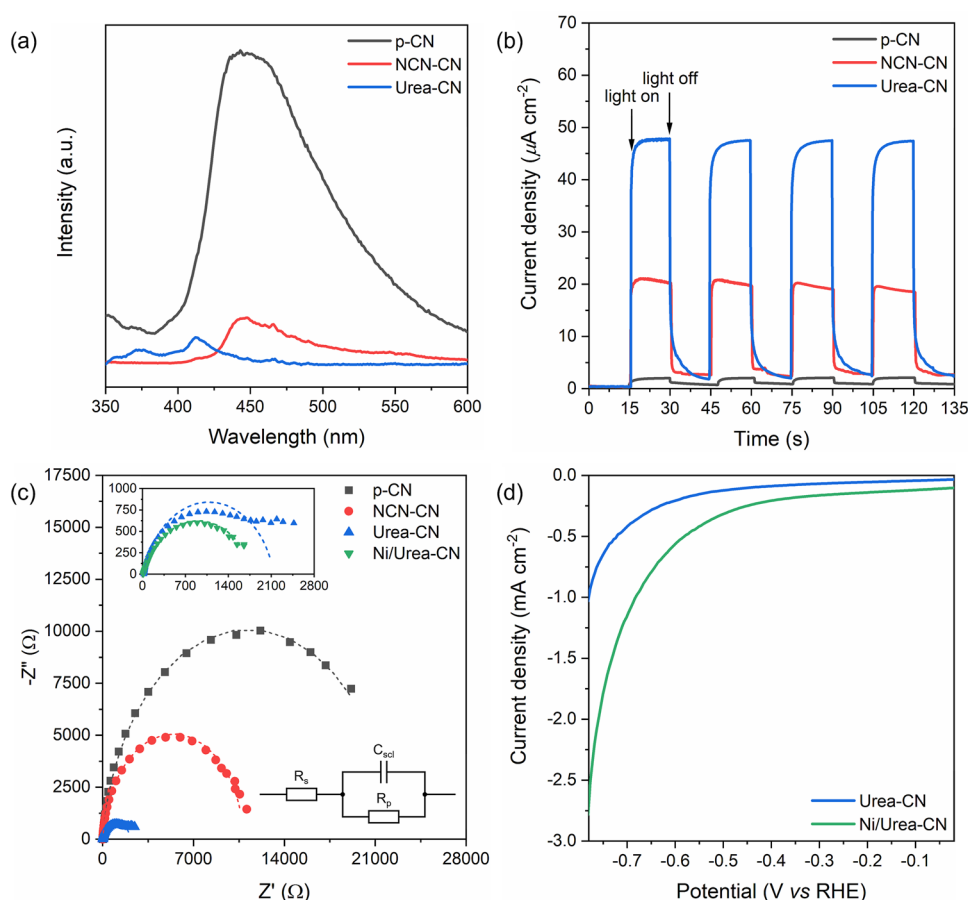
charge separation and transfer efficiency, which may be attributed to the electron-withdrawing effects of the O atom present in the urea groups [41].

Electrochemical impedance spectroscopy (EIS) was performed to further evaluate the charge transfer efficiency at the interface of the photocatalyst and electrolyte [42]. Nyquist plots for p-CN, NCN–CN, and Urea-CN are presented in Fig. 5c. The arc radius of the fitted Nyquist plot is proportional to the charge transfer impedance [43]. The calculated series resistance (R_s) and charge-transfer resistance (R_p) of FTO/electrode and electrode/electrolyte interfaces are summarized in Table S1. Urea-CN exhibits a noticeable decrease in the arc radius compared to p-CN and NCN–CN, indicating that the existence of urea functional groups is helpful for charge transfer. The improved charge transfer subsequently leads to accelerated interfacial electron and hole consumption in Urea-CN as evidenced by the lower charge transfer resistance at the photocatalyst/electrolyte interface (R_p) of Urea-CN (2.24 kΩ) compared to p-CN (22.38 kΩ) and NCN-CN (10.84 kΩ).

Time-resolved photoluminescence (TRPL) measurements were employed to examine the charge carrier kinetics, which can provide an insight into the interfacial electron transfer dynamics. The TRPL decay curves were obtained using a time-correlated single-photon counting technique with a pulsed laser at an excitation wavelength of 405 nm. To determine the charge lifetimes, the TRPL decay curves of p-CN, NCN–CN, and Urea-CN (Fig. S11) were fitted with biexponential functions according to Eq. 2.

$$y_i = y_0 + A_1 e^{\frac{-(x-x_0)}{\tau_1}} + A_2 e^{\frac{-(x-x_0)}{\tau_2}}, \tag{2}$$

where A and τ are the amplitudes and lifetimes, respectively. All fitted kinetic parameters for p-CN, NCN-CN, and Urea-CN are summarized in Table S2. The TRPL decays for all carbon nitride samples are biexponential in which the fast decay components (τ_1) have a more prevalent contribution than the slow decay component (τ_2). The fast and slow TRPL decay components are ascribed to nonradiative and radiative recombination, respectively [44]. The charge transfer pathway leading to H_2 evolution can be considered as an efficient nonradiative channel [23]. The average lifetimes are calculated for p-CN, NCN-CN, and Urea-CN according to Eq. 3.

$$\tau_{av} = \frac{A_1 \tau_1^2 + A_2 \tau_2^2}{A_1 \tau_1 + A_2 \tau_2}. \tag{3}$$

The average lifetime for Urea-CN (0.476 ns) is significantly lower than that for p-CN (1.345 ns), indicating a faster nonradiative recombination rate in Urea-CN than in p-CN. NCN-CN, which has been identified as having a strong electron-storing property [21], and possesses a shorter average

lifetime (0.374 ns) than Urea-CN. However, the shorter average charge carrier lifetime of NCNCN did not lead to a higher photocatalytic performance compared to Urea-CN. The prevalent electron-storing property of NCNCN could hinder electron consumption in the absence or limited presence of electron scavengers, thus delivering diminished photoelectrochemical characteristics and photocatalytic performance.

In the presence of Ni as an H_2 evolution cocatalyst, electron transfer is expected to be significantly improved as observed from the enhanced ethanol photoreforming performance by Ni/Urea-CN. The EIS spectrum of Ni/Urea-CN in the Fig. 5c inset suggests that the presence of the Ni cocatalyst assists with improving the interfacial charge transfer. Based on its fiitted Nyquist plot, the charge transfer resistance at the interface between Ni/Urea-CN and the electrolyte is calculated to be 1.79 kΩ, which is lower than that for Urea-CN. To further verify the enhanced electron transfer by the Ni cocatalyst, cathodic linear sweep voltammetry (LSV) was conducted on the Urea-CN and Ni/Urea-CN samples. Figure 5d shows that the LSV response of Ni/Urea-CN under dark conditions exhibits a more negative cathodic current density compared to the Urea-CN. For instance, at an applied potential of − 0.7 V vs RHE, Ni/Urea-CN exhibits a current density of − 0.92 mA cm^{-2}, which is more than twofold higher than for Urea-CN (− 0.37 mA cm^{-2}). This indicates that the Ni cocatalyst can assist with accelerating electron uptake for the H_2 evolution reaction.

Mott–Schottky measurements were also conducted on Urea-CN and Ni/Urea-CN (Fig. S12). The donor densities are calculated from the slopes of the obtained Mott–Schottky plots. Based on the Mott–Schottky equation (Eq. 4), the donor density (N_D) is inversely proportional to the slope while the x-intercept represents the flatband potential (V_{fb}) [45].

$$\frac{1}{C_{scl}^2} = \frac{2}{\varepsilon_s \varepsilon_0 A^2 e N_D} \left(V - V_{fb} - \frac{k_B T}{e} \right), \tag{4}$$

where C_{scl} is the space-charge capacitance of the semiconductor, ε_s is the dielectric constant of the semiconductor (7.17–8.05 for carbon nitride thin film; median value of 7.61 is used) [46], ε_0 is the permittivity of free space, A is the area of the interface, e is the electron charge, V is the applied potential, V_{fb} is the flatband potential, k_B is Boltzmann's constant, T is the absolute temperature. Ni/Urea-CN exhibits an enhanced donor density of 7.80×10^{26} m^{-3} compared to Urea-CN (5.70×10^{26} m^{-3}), indicating an accelerated electron transfer from Urea-CN to Ni. In addition, a positive shift of the flatband potential for Ni/Urea-CN is mainly due to the Ni cocatalyst which may alter the equilibrium of the Fermi level position. This creates a band bending structure at the Ni and Urea-CN junction [47].

Based on the photoelectrochemical characterization results, we propose a mechanism for ethanol photoreforming on the Ni/Urea-CN photocatalyst. Under light irradiation, Urea-CN is activated to form electrons and holes. Subsequently, these charge carriers migrate to the photocatalyst surface and are attracted by the electron-withdrawing O moiety in the urea groups, preventing recombination with the holes. The electrons are then transferred to the Ni cocatalyst for H_2 evolution. Concurrently, the mobile photogenerated holes in the energetic valence band of Urea-CN invoke the accelerated selective ethanol oxidation into acetaldehyde.

The enhanced crystallinity and specific surface area of carbon nitride may also contribute to the carrier dynamics improvement. Upon the introduction of cyanamide functional groups, NCN-CN exhibits a higher crystallinity than p-CN as shown by the XRD patterns in Fig. 1b. The crystallinity improvement is attributed to the ability of cyanamide groups to induce further polymerization of heptazine rings as well as the presence of potassium cations that lead to a more ordered stacking [33]. Interestingly, the crystallinity of Urea-CN remains high after acid-catalyzed hydrolysis. In crystalline carbon nitride, the photogenerated electrons and holes typically exhibit higher mobility, thus leading to improved charge migration from the bulk to the surface. Concomitantly, the protons in solution during hydrolysis treatment may intercalate between the carbon nitride layers and subsequently exfoliate the structure. The exfoliation effect is evident from the significantly higher specific surface area of Urea-CN (101.5 m^2 g^{-1}) compared to p-CN (15.6 m^2 g^{-1}) and NCNCN (57.7 m^2 g^{-1}). The improved specific surface area of Urea-CN facilitates more rapid consumption of electrons and holes on the surface, preventing severe charge carrier recombination.

4 Conclusions

In summary, an in situ photodeposited Ni on urea-functionalized carbon nitride (Ni/Urea-CN) has been demonstrated to improve ethanol photoreforming performance. In the presence of a 1 mM Ni^{2+} precursor concentration, Ni/Urea-CN delivered an H_2 evolution rate of 760.5 μmol h^{-1} g^{-1} in conjuction with an acetaldehyde production rate of 888.2 μmol h^{-1} g^{-1}. Introducing the urea groups was shown to improve carrier dynamics in the carbon nitride photocatalyst due to the electron-withdrawing effect of the O moiety in the urea groups. In addition, Urea-CN possesses high crystallinity and specific surface area, enabling rapid charge carrier migration and transfer as evidenced by the photoelectrochemical characterization findings. As a result, electron transfer from the Urea-CN to the Ni cocatalyst for H_2 evolution and the hole transfer for ethanol oxidation are improved, delivering an overall enhanced performance.

Declarations

References

1. Chen, S., Takata, T., & Domen, K. (2017). Particulate photocatalysts for overall water splitting. *Nat Rev Mater*. https://doi.org/10.1038/natrevmats.2017.50

2. Takata, T., & Domen, K. (2019). Particulate photocatalysts for water splitting: recent advances and future prospects. *ACS Energy Letters, 4*, 542–549. https://doi.org/10.1021/acsenergylett.8b02209

3. Hisatomi, T., & Domen, K. (2019). Reaction systems for solar hydrogen production via water splitting with particulate semiconductor photocatalysts. *Nature Catalysis, 2*, 387–399. https://doi.org/10.1038/s41929-019-0242-6

4. Pinaud, B. A., Benck, J. D., Seitz, L. C., Forman, A. J., Chen, Z., Deutsch, T. G., James, B. D., Baum, K. N., Baum, G. N., Ardo, S., Wang, H., Miller, E., & Jaramillo, T. F. (2013). Technical and economic feasibility of centralized facilities for solar hydrogen production via photocatalysis and photoelectrochemistry. *Energy & Environmental Science*. https://doi.org/10.1039/c3ee40831k

5. Reisner, E. (2019). When does organic photoredox catalysis meet artificial photosynthesis? *Angewandte Chemie International Edition, 58*, 3656–3657. https://doi.org/10.1002/anie.201814692

6. Uekert, T., Pichler, C. M., Schubert, T., & Reisner, E. (2020). Solar-driven reforming of solid waste for a sustainable future. *Nat Sustain, 4*, 383–391. https://doi.org/10.1038/s41893-020-00650-x

7. Ramis, G., Bahadori, E., & Rossetti, I. (2021). Design of efficient photocatalytic processes for the production of hydrogen from biomass derived substrates. *International Journal of Hydrogen Energy, 46*, 12105–12116. https://doi.org/10.1016/j.ijhydene.2020.02.192

8. Chiarello, G. L., Dozzi, M. V., Scavini, M., Grunwaldt, J.-D., & Selli, E. (2014). One step flame-made fluorinated Pt/TiO$_2$ photocatalysts for hydrogen production. *Applied Catalysis B: Environmental, 160–161*, 144–151. https://doi.org/10.1016/j.apcatb.2014.05.006

9. Toe, C. Y., Tsounis, C., Zhang, J., Masood, H., Gunawan, D., Scott, J., & Amal, R. (2021). Advancing photoreforming of organics: highlights on photocatalyst and system designs for selective oxidation reactions. *Energy & Environmental Science, 14*, 1140–1175. https://doi.org/10.1039/d0ee03116j

10. Rosales-Calderon, O., & Arantes, V. (2019). A review on commercial-scale high-value products that can be produced alongside cellulosic ethanol. *Biotechnology for Biofuels, 12*, 240. https://doi.org/10.1186/s13068-019-1529-1

11. Verified Market Research (2022). Acetaldehye market size and forecast USA; Report No.: 8008.

12. Wang, J., Kumar, P., Zhao, H., Kibria, M. G., & Hu, J. (2021). Polymeric carbon nitride-based photocatalysts for photoreforming of biomass derivatives. *Green Chemistry, 23*, 7435–7457. https://doi.org/10.1039/d1gc02307a

13. Ong, W. J., Tan, L. L., Ng, Y. H., Yong, S. T., & Chai, S. P. (2016). Graphitic carbon nitride (g-C$_3$N$_4$)-based photocatalysts for artificial photosynthesis and environmental remediation: are we a step closer to achieving sustainability? *Chemical Reviews, 116*, 7159–7329. https://doi.org/10.1021/acs.chemrev.6b00075

14. Wang, Y., Phua, S. Z. F., Dong, G., Liu, X., He, B., Zhai, Q., Li, Y., Zheng, C., Quan, H., Li, Z., & Zhao, Y. (2019). Structure tuning of polymeric carbon nitride for solar energy conversion: from nano to molecular scale. *Chem, 5*, 2775–2813. https://doi.org/10.1016/j.chempr.2019.07.019

15. Liu, J., Liu, Y., Liu, N., Han, Y., Zhang, X., Huang, H., Lifshitz, Y., Lee, S., Zhong, J., & Kang, Z. (2015). Metal-free efficient photocatalyst for stable visible water splitting via a two-electron pathway. *Science, 347*, 970–974. https://doi.org/10.1126/science.aaa3145

16. Cao, S., Low, J., Yu, J., & Jaroniec, M. (2015). Polymeric photocatalysts based on graphitic carbon nitride. *Advanced Materials, 27*, 2150–2176. https://doi.org/10.1002/adma.201500033

17. Zhou, Z., Zhang, Y., Shen, Y., Liu, S., & Zhang, Y. (2018). Molecular engineering of polymeric carbon nitride: advancing applications from photocatalysis to biosensing and more. *Chemical Society Reviews, 47*, 2298–2321. https://doi.org/10.1039/c7cs00840f

18. Jimenez-Salcedo, M., Monge, M., & Tena, M. T. (2022). An organometallic approach for the preparation of Au-TiO$_2$ and Au-g-C$_3$N$_4$ nanohybrids: Improving the depletion of paracetamol under visible light. *Photochemical & Photobiological Sciences, 21*, 337–347. https://doi.org/10.1007/s43630-022-00172-9

19. Li, Y., Li, X., Zhang, H., Fan, J., & Xiang, Q. (2020). Design and application of active sites in g-C$_3$N$_4$-based photocatalysts. *Journal of Materials Science & Technology, 56*, 69–88. https://doi.org/10.1016/j.jmst.2020.03.033

20. Liu, J., Fu, W., Liao, Y., Fan, J., & Xiang, Q. (2021). Recent advances in crystalline carbon nitride for photocatalysis. *Journal of Materials Science & Technology, 91*, 224–240. https://doi.org/10.1016/j.jmst.2021.03.017

21. Gunawan, D., Toe, C. Y., Kumar, P., Scott, J., & Amal, R. (2021). Synergistic cyanamide functionalization and charge-induced activation of nickel/carbon nitride for enhanced selective photoreforming of ethanol. *ACS Applied Materials & Interfaces, 13*, 49916–49926. https://doi.org/10.1021/acsami.1c14195

22. Kasap, H., Caputo, C. A., Martindale, B. C., Godin, R., Lau, V. W., Lotsch, B. V., Durrant, J. R., & Reisner, E. (2016). Solar-driven reduction of aqueous protons coupled to selective alcohol oxidation with a carbon nitride-molecular Ni catalyst system. *Journal of the American Chemical Society, 138*, 9183–9192. https://doi.org/10.1021/jacs.6b04325

23. Lau, V.W.-H., Yu, V.W.-Z., Ehrat, F., Botari, T., Moudrakovski, I., Simon, T., Duppel, V., Medina, E., Stolarczyk, J. K., Feldmann, J., Blum, V., & Lotsch, B. V. (2017). Urea-modified carbon nitrides: enhancing photocatalytic hydrogen evolution by rational defect engineering. *Advanced Energy Materials.* https://doi.org/10.1002/aenm.201602251

24. Ferre-Vilaplana, A., Buso-Rogero, C., Feliu, J. M., & Herrero, E. (2016). Cleavage of the C–C bond in the ethanol oxidation reaction on platinum. Insight from experiments and calculations. *Journal of Physical Chemistry C, 120*, 11590–11597. https://doi.org/10.1021/acs.jpcc.6b03117

25. Lau, V. W., Moudrakovski, I., Botari, T., Weinberger, S., Mesch, M. B., Duppel, V., Senker, J., Blum, V., & Lotsch, B. V. (2016). Rational design of carbon nitride photocatalysts by identification of cyanamide defects as catalytically relevant sites. *Nature Communications, 7*, 12165. https://doi.org/10.1038/ncomms12165

26. Abdullah, M., Low, G.K.-C., & Matthews, R. W. (1990). Effects of common inorganic anions on rates of photocatalytic oxidation of organic carbon over illuminated titanium dioxide. *Journal of Physical Chemistry, 94*, 6820–6825. https://doi.org/10.1021/j100380a051

27. Hatchard, C. G., & Parker, C. A. (1956). A new sensitive chemical actinometer II. Potassium ferrioxalate as a standard chemical actinometer. *Proceedings: Mathematical, Physical and Engineering Sciences, 235*, 518–536. https://doi.org/10.1098/rspa.1956.0102

28. Kasap, H., Godin, R., Jeay-Bizot, C., Achilleos, D. S., Fang, X., Durrant, J. R., & Reisner, E. (2018). Interfacial Engineering of a Carbon Nitride-Graphene Oxide–Molecular Ni Catalyst Hybrid for Enhanced Photocatalytic Activity. *ACS Catalysis, 8*, 6914–6926. https://doi.org/10.1021/acscatal.8b01969

29. Wu, X., Ng, Y. H., Saputera, W. H., Wen, X., Du, Y., Dou, S. X., Amal, R., & Scott, J. (2019). The Dependence of Bi$_2$MoO$_6$ Photocatalytic Water Oxidation Capability on Crystal Facet Engineering. *ChemPhotoChem, 3*, 1246–1253. https://doi.org/10.1002/cptc.201900113

30. Scaife, D. E. (1980). Oxide Semiconductors in Photoelectrochemical Conversion of Solar Energy. *Solar Energy, 25*, 41–54.

31. Wu, X., Xie, S., Zhang, H., Zhang, Q., Sels, B. F., & Wang, Y. (2021). Metal Sulfide Photocatalysts for Lignocellulose Valorization. *Advanced Materials, 33*, e2007129. https://doi.org/10.1002/adma.202007129

32. Lau, V. W., Klose, D., Kasap, H., Podjaski, F., Pignie, M. C., Reisner, E., Jeschke, G., & Lotsch, B. V. (2017). Dark photocatalysis: storage of solar energy in carbon nitride for time-delayed hydrogen generation. *Angewandte Chemie, 56*, 510–514. https://doi.org/10.1002/anie.201608553

33. Schlomberg, H., Kroger, J., Savasci, G., Terban, M. W., Bette, S., Moudrakovski, I., Duppel, V., Podjaski, F., Siegel, R., Senker, J., Dinnebier, R. E., Ochsenfeld, C., & Lotsch, B. V. (2019). Structural insights into poly(heptazine imides): a light-storing carbon nitride material for dark photocatalysis. *Chemistry of Materials, 31*, 7478–7486. https://doi.org/10.1021/acs.chemmater.9b02199

34. Lovell, E. C., Lu, X., Zhang, Q., Scott, J., & Amal, R. (2020). From passivation to activation—tunable nickel/nickel oxide for hydrogen evolution electrocatalysis. *Chemical Communications (Cambridge, England), 56*, 1709–1712. https://doi.org/10.1039/c9cc07486d

35. Tsounis, C., Lu, X., Bedford, N. M., Subhash, B., Thomsen, L., Zhang, Q., Ma, Z., Ostrikov, K. K., Bendavid, A., Scott, J. A., Amal, R., & Han, Z. (2020). Valence alignment of mixed Ni-Fe

hydroxide electrocatalysts through preferential templating on graphene edges for enhanced oxygen evolution. *ACS Nano, 14*, 11327–11340. https://doi.org/10.1021/acsnano.0c03380

36. Wang, Z., Fan, J., Cheng, B., Yu, J., & Xu, J. (2020). Nickel-based cocatalysts for photocatalysis: Hydrogen evolution, overall water splitting and CO_2 reduction. *Materials Today Physics*. https://doi.org/10.1016/j.mtphys.2020.100279

37. Cao, S., & Piao, L. (2020). Considerations for a more accurate evaluation method for photocatalytic water splitting. *Angewandte Chemie (International ed. in English), 59*, 18312–18320. https://doi.org/10.1002/anie.202009633

38. Melchionna, M., & Fornasiero, P. (2020). Updates on the roadmap for photocatalysis. *ACS Catalysis, 10*, 5493–5501. https://doi.org/10.1021/acscatal.0c01204

39. Wang, Z., Hisatomi, T., Li, R., Sayama, K., Liu, G., Domen, K., Li, C., & Wang, L. (2021). Efficiency accreditation and testing protocols for particulate photocatalysts toward solar fuel production. *Joule, 5*, 344–359. https://doi.org/10.1016/j.joule.2021.01.001

40. Yuan, J., Tang, Y., Yi, X., Liu, C., Li, C., Zeng, Y., & Luo, S. (2019). Crystallization, cyanamide defect and ion induction of carbon nitride: exciton polarization dissociation, charge transfer and surface electron density for enhanced hydrogen evolution. *Applied Catalysis B: Environmental, 251*, 206–212. https://doi.org/10.1016/j.apcatb.2019.03.069

41. Bai, J. Y., Wang, L. J., Zhang, Y. J., Wen, C. F., Wang, X. L., & Yang, H. G. (2020). Carboxyl functionalized graphite carbon nitride for remarkably enhanced photocatalytic hydrogen evolution. *Applied Catalysis B: Environmental*. https://doi.org/10.1016/j.apcatb.2020.118590

42. Xu, W., Gao, W., Meng, L., Tian, W., & Li, L. (2021). Incorporation of sulfate anions and sulfur vacancies in $ZnIn_2S_4$ Photoanode for enhanced photoelectrochemical water splitting. *Advanced Energy Materials*. https://doi.org/10.1002/aenm.202101181

43. Chung, H. Y., Toe, C. Y., Chen, W., Wen, X., Wong, R. J., Amal, R., Abdi, F. F., & Ng, Y. H. (2021). Manipulating the fate of charge carriers with tungsten concentration: enhancing photoelectrochemical water oxidation of Bi_2WO_6. *Small (Weinheim an der Bergstrasse, Germany), 17*, e2102023. https://doi.org/10.1002/smll.202102023

44. Xing, Y., Wang, L., Yang, D., Wang, Z., Hao, Z., Sun, C., Xiong, B., Luo, Y., Han, Y., Wang, J., & Li, H. (2017). A novel model on time-resolved photoluminescence measurements of polar InGaN/GaN multi-quantum-well structures. *Science and Reports, 7*, 45082. https://doi.org/10.1038/srep45082

45. Toe, C. Y., Tan, H. L., Boyer, C., Rawal, A., Thickett, S. C., Scott, J., Amal, R., & Ng, Y. H. (2017). Photo-driven synthesis of polymer-coated platinized ZnO nanoparticles with enhanced photoelectrochemical charge transportation. *J Mater Chem A, 5*, 4568–4575. https://doi.org/10.1039/c6ta10665j

46. Patra, P. C., & Mohapatra, Y. N. (2021). Dielectric constant of thin film graphitic carbon nitride (g-C_3N_4) and double dielectric Al_2O_3/g-C_3N_4. *Applied Physics Letters*. https://doi.org/10.1063/5.0045911

47. Guerrero-Araque, D., Ramírez-Ortega, D., Calderon, H. A., Saniger, J. M., & Gómez, R. (2020). Effect of Co-catalyst (CuO, CoO or NiO) on Bi_2O_3–TiO_2 Structures and Its Impact on the Photocatalytic Reduction of 4-Nitrophenol. *Topics in Catalysis, 64*, 112–120. https://doi.org/10.1007/s11244-020-01335-7

Authors and Affiliations

Denny Gunawan[1] · **Cui Ying Toe[1,2]** · **Kaiwen Sun[3]** · **Jason Scott[1]** · **Rose Amal[1]**

1   Particles and Catalysis Research Group, School of Chemical Engineering, The University of New South Wales (UNSW), Sydney, NSW 2052, Australia

2   School of Engineering, The University of Newcastle, Callaghan, NSW 2308, Australia

3   School of Photovoltaic and Renewable Energy Engineering, The University of New South Wales (UNSW), Sydney, NSW 2052, Australia